Quantification of 3D Left Ventricular Deformation using Hyperelastic Warping: Comparisons between MRI and PET Imaging

AI Veress*, JA Weiss*, GJ Klein+, GT Gullberg+

+Lawrence Berkeley National Laboratory, Berkeley, California, USA
*University of Utah, Salt Lake City, Utah, USA

Abstract

Image based finite element (FE) analysis was used to determine the deformation of the left ventricle (LV) between end-systole and end-diastole. The algorithm used volumetric MRI data to create a body force that deformed a finite element model of the LV over half of the cardiac cycle and tracked the tissue deformation. The accuracy of the computational predictions of strain were assessed by the creation of image data sets for which displacements between the images were known. A "forward" left ventricular FE model was given physiological loading and material properties. A loaded magnetic resonance imaging (MRI) data set was created by displacing the end-systolic image MRI data set using the displacement values determined from the forward model. The strains computed from the forward and Warping solutions were compared. Further, PET images from a single patient were analyzed and compared to MRI-based Warping analysis results for the same patient at mid-ventricle and at the base of the LV. The fiber stretch distribution between the forward and warping solutions show good agreement, both in overall stretch distribution and for the stretch values on the image planes. The MRI and PET analyses showed similar stretch distributions indicating that strain distributions can be measured from PET images.

1. Introduction

Assessment of regional heart wall motion (wall motion, thickening, strain) can provide quantitative information regarding ventricular wall function, can localize ischemic myocardial disease and can identify impairment of cardiac function due to hypertrophic or dilated cardiomyopathies. Our long-term goal is to improve the diagnosis and treatment of these pathologies by developing validated techniques that will allow determination of the changes in strain distribution resulting from these conditions.

The development of MRI tagging techniques has made it possible to perform non-invasive measurements of myocardial wall dynamics [1]. The MRI tagging technique relies on local perturbation of the magnetization of the myocardium with selective radio-frequency (RF) saturation to produce multiple, thin tag planes during diastole. The resulting magnetization reference grid persists for up to 400 ms and is convected with the myocardium as it deforms. This is followed by conventional, orthogonal-plane imaging during systole [2]. The tags provide fiducials from which the deformation gradient and strain tensors can be calculated [3, 4]. The tags are usually laid down as a rectilinear grid, using image acquisition that is gated to the ECG to acquire multiple slices and thus form a 3D dataset.

Although MRI tagging is effective for tracking fast, repeated motions in 3D, major limitations of the technique for cardiac imaging are its spatial resolution, which is much coarser than the MRI acquisition matrix, and the lengthy image acquisition time. Furthermore, these methods cannot be used with other imaging modalities such as Positron Emission Tomography (PET) or Single-Photon Computed Tomography (SPECT), which cannot be altered to allow for the addition of fiducial points to track the strain within the myocardial wall.

We have developed an image based finite element technique known as Warping that allows the extraction of strain information from sequences of images of a deforming tissue without markers [5]. The present work addresses the validation of the use of Warping with cine MRI data to determine the fiber strain distribution of the left ventricle during the cardiac cycle. Additionally, the fiber stretch distribution for a normal left ventricle from end-systole to end-diastole was determined using Warping and cine MRI image data sets. These results were compared with the stretch distribution determined the Warping analysis of a PET image data set of the same individual.

2. Methods

2.1. Warping theory

A brief description of the Warping technique for deformable image registration is provided below. Additional details can be found in previous publications [5,

6]. The approach requires an image of the tissue in a reference configuration (*template* image), and an image in the deformed configuration (*target* image). The Warping technique produces a position-dependent body force from the pointwise intensity differences between the images. The body force is applied to a finite element (FE) representation of the object of interest in the template image, causing it to deform into registration with the target image. The Warping body force is derived from an image-based energy density U defined as the pointwise difference in intensities between the template and target images:

$$U(\mathbf{X},\boldsymbol{\varphi}) = \frac{\lambda}{2}\left(T(\mathbf{X},\boldsymbol{\varphi}) - S(\mathbf{X},\boldsymbol{\varphi})\right)^2 \qquad (1)$$

Here, $\boldsymbol{\varphi}(\boldsymbol{X})$ is the deformation map applied to the template image, $\boldsymbol{X}$ represents the reference coordinates of a material point in the template, T and S are the scalar template and target image intensities at a point in the domain of the deformed template, and λ is a penalty parameter that enforces the constraint. The total energy of the continuum, $E(\boldsymbol{\varphi})$, is defined as the sum of the image-based energy density and the standard strain energy density for a hyperelastic material, $W(\boldsymbol{X},\boldsymbol{C})$:

$$E(\boldsymbol{\varphi}) = \int_B W(\mathbf{X},\mathbf{C}(\boldsymbol{\varphi}(\mathbf{X})))dV + \int_B U(\mathbf{X},\boldsymbol{\varphi}(\mathbf{X}))dV \qquad (2)$$

Here, $\boldsymbol{C}$ is the right deformation tensor.

At equilibrium, the total energy in the system is minimized and the internal material forces due to the stress divergence balance with those that arise from the image-based energy term. The first variation of $E(\boldsymbol{\varphi})$ with respect to $\boldsymbol{\varphi}$ yields the modified equilibrium equations for the continuum [5]. An image-based force term arises:

$$\frac{\partial U}{\partial \boldsymbol{\varphi}} = \lambda\left(T(\mathbf{X},\boldsymbol{\varphi}(\mathbf{X})) - S(\mathbf{X},\boldsymbol{\varphi}(\mathbf{X}))\right)\left(\frac{\partial T}{\partial \boldsymbol{\varphi}} - \frac{\partial S}{\partial \boldsymbol{\varphi}}\right) \qquad (3)$$

This vector term is a position- and deformation-dependent body force that attempts to simultaneously minimize local differences in image intensity and intensity gradients between the template and target images. The image gradients provide the local direction information for the force vector. The image data do not contribute any forces when either the difference in image intensities is zero or the difference between the image intensity gradients is zero (Equation 3).

2.2. Sequential spatial filtering

The Warping technique is susceptible to local minima. The registration process may get "stuck" by alignment of local image inhomogeneities that prevent global image alignment. We develop an approach to first register larger image features such as object boundaries and coarse textural detail, followed by registration of fine detail, by employing sequential spatial filtering. By evolving the sharpness of the image over quasi-time, one can control the influence of fine textural features in the image until global registration is achieved. Sequential spatial smoothing with a Gaussian mask was used for both the template and target images in the analyses for this study [7].

2.3. Image acquisition

Gated cine MRI images were acquired on a 1.5T Siemens scanner (256x256 image matrix, 378 mm FOV, 10 mm slice thickness, 10 slices). The gated PET data were acquired on a CTI/Siemens ECAT EXACT HR scanner using the radiotracer 18F-fluorodeoxyglucose (256x256 image matrix, 378 mm FOV, 10 mm slice thickness, 10 slices). Emission data were collected for 20 to 60 minutes and images were reconstructed at 40 msec intervals. The volumetric MRI and PET datasets corresponding to end-systole were designated as the template images and image datasets corresponding to end-diastole were designated the target images.

2.4. Geometry extraction from image data

The 2D contours of the left ventricular endocardial and epicardial surfaces were segmented manually from the end-systolic PET and MRI image datasets to create the FE models. The contours were imported into a commercial mesh generation program (TrueGrid, XYZ Scientific Applications, Livermore, CA) to create the FE models. For both models, the myocardium was represented as a transversely isotropic material with the fiber angle varying from –90° at the epicardial surface, through 0° at the midwall, to 90° at the endocardial surface. The material properties of the myocardial wall were determined from least squares curve fits of the biaxial test data reported by Humphrey et al. [8, 9].

2.5. Warping solution procedure

The Warping analysis consisted of two phases. During the first phase of the analysis, the penalty parameter λ was increased gradually over quasi-time while the amount of spatial filtering remained constant, thus providing a means to evolve the image-derived forces on the model and achieve global registration of the deforming template with the target image. In the second phase, the penalty was held fixed while the amount of spatial filtering was reduced to achieve local registration.

2.6. Warping validation

To test the efficacy of Warping for prediction of strains from cine MRI images, a pair of 3-D MRI image datasets representing two deformation states of a left ventricle was required. Additionally, the deformation map between the states represented in the images had to be known. To achieve this, a FE model of the left ventricle (LV) was created from the end-systolic MRI

image data set. A 55 mmHg (7.3 KPa) internal pressure load was applied to the lumen and a standard FE analysis was performed. This analysis yielded the strains in the loaded LV, the "forward" FE solution for the strain distribution in the ventricle, which was similar to the distributions found in literature [10]. Using the displacement results from the forward FE analysis, a deformed image (*target*) was created by applying the displacement map to the original template MRI image. Warping analysis was then performed using the undeformed and deformed images. No other loads were placed on the models but those derived from the image datasets. The forward and Warping predictions of fiber stretch (final length/initial length along the local fiber direction) were compared to determine the accuracy of the technique.

2.7. Analysis of PET and MRI image data sets

To compare results for prediction of fiber stretch from MRI and PET image datasets, Warping analyses were conducted using both the MRI and PET-based FE models and the end-systolic and end-diastolic image data sets for each modality. The models were analyzed and the fiber stretch results were compared. Again, no other loads were placed on the models but those derived from the image data sets.

3. Results

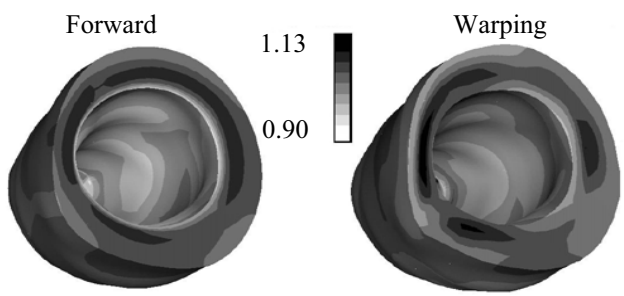

Figure 1. Fiber stretch distribution for the forward (left) and warping (right) analysis. Distributions show good agreement.

3.1. Validation results

The validation results indicate good agreement between the forward and the warping fiber stretch distributions (Figure 1). A detailed analysis of the forward and predicted (Warping) stretch distributions for each image plane indicates excellent agreement (Figure 2).

3.2. MRI and PET results

The results for the PET and MRI analyses indicate that

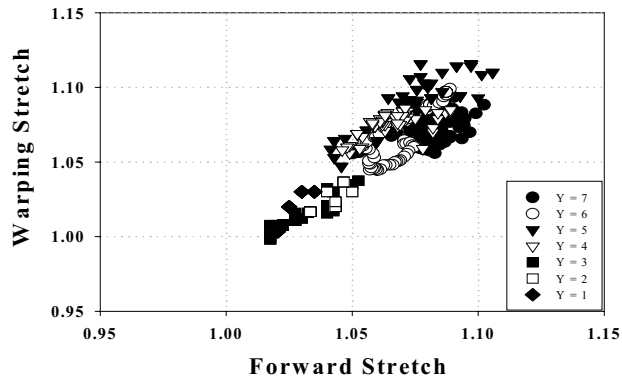

Figure 2. Comparison of Warping and forward solutions for each image layer. Y = 7 corresponds to the layer at the base of the LV and Y = 1 is near the apex of the heart.

Warping of the PET images resulted in stretch distributions that were similar to the stretch distributions determined by the warping analysis of the MRI data (Figure 3). The average of the circumferential fiber stretch values showed a 9% difference between the

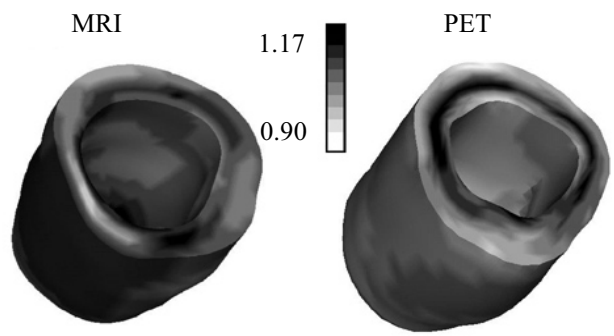

Figure 3. Fiber stretch distribution for the MRI (left) and PET (right) analysis. Distributions show reasonable agreement.

modalities at the base and mid-ventricular area. For the base slice, the average circumferential stretch for the MRI analysis was 1.12 while the average circumferential stretch for the PET analysis was 1.11 Similarly, the results for the mid-ventricle area showed nearly exactly the same average circumferential stretch (1.11 for MRI and 1.10 for PET). The overall length change in the MRI analysis was found to be 1.0 cm while none was measured for the PET analysis.

4. Discussion

The overall results for stretch distribution and the results for comparisons on specific image planes showed good agreement between the forward and Warping solutions. This indicates that warping can accurately predict the stretch distributions from cine MRI images.

The PET results showed similar fiber stretch distributions as for the MRI analysis, but there were substantial differences for the longitudinal stretch

determined from each analysis. The longitudinal PET and MRI results indicate that the between-plane resolution of 1 cm is too large to make accurate determination of the motion of the heart in the longitudinal direction. The PET analysis results indicated no change in length while the MRI analysis indicated a 1 cm change in length.

Warping has two advantages over tagged MRI analyses. Warping has a higher spatial resolution than tagged analysis. The finite element mesh density can be refined to near the spatial resolution of the image if sufficient computational resources are available. Furthermore, untagged image datasets require a shorter acquisition time than required for a full 3-D tagged image dataset, a distinct advantage for analysis of patients with myocardial damage, since the length of time that they may lie supine is very limited.

The results of this study demonstrate that Warping can be used with both MRI and PET data to provide estimates of fiber stretch in the ventricular wall during diastole. This provides a mean to monitor ventricular deformation noninvasively without the use of MRI tagging techniques. Work in progress will compare fiber stretch predictions from MRI tagging and Warping by obtaining both tagged and untagged MRI datasets from a single healthy individual.

Acknowledgements

NIH #RO1HL39792 and NSF #BES-0134503.

References

[1] Ozturk C and McVeigh ER. Four-dimensional B-spline based motion analysis of tagged MR images: introduction and in vivo validation. Phys Med Biol 2000;45:1683-702.

[2] McVeigh ER and Zerhouni EA. Noninvasive measurement of transmural gradients in myocardial strain with MR imaging. Radiology 1991;180:677-83.

[3] Ungacta FF, Davila-Roman VG, Moulton MJ, Cupps BP, Moustakidis P, Fishman DS, Actis R, Szabo BA, Li D, Kouchoukos NT, and Pasque MK. MRI-radiofrequency tissue tagging in patients with aortic insufficiency before and after operation. Ann Thorac Surg 1998;65:943-50.

[4] Buchalter MB, Weiss JL, Rogers WJ, Zerhouni EA, Weisfeldt ML, Beyar R, and Shapiro EP. Noninvasive quantification of left ventricular rotational deformation in normal humans using magnetic resonance imaging myocardial tagging. Circulation 1990;81:1236-44.

[5] Weiss JA, Rabbitt RD, and Bowden AE. Incorporation of medical image data in finite element models to track strain in soft tissues. SPIE 1998;3254:477-484.

[6] Rabbitt RD, Weiss JA, Christensen GE, and Miller MI. Mapping of hyperelastic deformable templates using the finite element method. SPIE 1995;2573:252-265.

[7] Veress AI, Weiss JA, Gullberg GT, Vince DG, and Rabbitt RD. Strain Measurement in Coronary Arteries Using Intravascular Ultrasound and Deformable Images. J Biomech Eng 2002;(in press).

[8] Humphrey JD, Strumpf RK, and Yin FC. Determination of a constitutive relation for passive myocardium: II. Parameter estimation. J Biomech Eng 1990;112:340-6.

[9] Humphrey JD, Strumpf RK, and Yin FC. Determination of a constitutive relation for passive myocardium: I. A new functional form. J Biomech Eng 1990;112:333-9.

[10] Tseng WY, Reese TG, Weisskoff RM, Brady TJ, and Wedeen VJ. Myocardial fiber shortening in humans: initial results of MR imaging. Radiology 2000;216:128-39.

Address for correspondence:
Alexander I. Veress, Ph.D.
MIRL, 729 Arapeen Drive
Salt Lake City, UT 84108-1218, USA
averess@doug.med.utah.edu